



Untangling the Origin of Molecular Hydrogen in the Lunar Exosphere

Parker B. Crandall^{1,2} , Jeffrey J. Gillis-Davis^{3,4} , and Ralf I. Kaiser^{1,2} 

¹Department of Chemistry, University of Hawai'i at Mānoa, Honolulu, HI 96822, USA; ralfk@hawaii.edu

²W. M. Keck Laboratory in Astrochemistry, University of Hawai'i at Mānoa, Honolulu, HI 96822, USA

³Hawai'i Institute of Geophysics and Planetology, University of Hawai'i at Mānoa, Honolulu, HI 96822, USA

Received 2019 June 15; revised 2019 October 9; accepted 2019 October 9; published 2019 December 6

Abstract

In situ experiments from the Apollo missions confirmed the presence of a tenuous exosphere on the Moon comprised of atoms and light molecular species. Of the most prominent volatiles found in the exosphere, molecular hydrogen (H_2) has drawn considerable attention because the confirmed detection of surface water has led many scientists to believe that proton bombardment of silicate minerals from the solar wind is the mechanism by which this water forms. As molecular hydrogen formation is a competing mechanism to bound OH/ H_2O in the regolith, experimental studies are needed to determine the efficiency of molecular hydrogen formation from the solar wind. Here we show that, under simulated lunar conditions, the formation, storage, and release of molecular deuterium—as a proxy of molecular hydrogen—from deuterium implanted olivine is facile. Secondary ion mass spectrometry results reveal that diffusion processes also enrich grains with deuterium at depths beyond the maximum penetration depth of the incident ions close to 100 nm. In addition, the maximum yield of molecular deuterium escaping the amorphous rims under simulated lunar conditions strongly supports previous studies, which claim that the solar wind represents the dominant source of exospheric molecular hydrogen.

Unified Astronomy Thesaurus concepts: Space weather (2037); Lunar atmosphere (947); Laboratory astrophysics (2004); Solar wind (1534)

1. Introduction

In situ measurements of the Apollo landings taken by the cold cathode gauge experiments of Apollo 14 and 15 as well as the surface neutral mass spectrometer of Apollo 17 provided the first evidence of a lunar exosphere at a level of about 10^{-9} mbar consisting of atoms and light molecular species like argon, helium, neon, sodium, potassium, and hydrogen (NASA 1973; Stern 1999; Lucey 2006). The concentration of these species varies depending on the time of day and suggests that the solar wind represents the primary source for all but a few trace elements (Feldman & Morrison 1991; Sarantos et al. 2012; Colaprete et al. 2016). Of these volatiles, molecular hydrogen (H_2) has drawn considerable attention from the lunar science community as hydrogen is not only chemically reactive, but also represents the molecular constituent in highest abundance. The tenuous lunar atmosphere is therefore suggested to be critically connected to the formation of surface water (H_2O) and/or hydroxyl radicals (OH)—as detected via the $2.8 \mu\text{m}$ band by the Moon Mineralogy Mapper (M^3)—through exposure of silicates by the solar wind (Clark 2009; Pieters et al. 2009; Sunshine et al. 2009).

As solar wind protons encounter the Moon, protons are implanted into regolith grains at an average energy of typically 1 to 2 keV amu^{-1} and are also neutralized along the trajectories (Gnaser 1999; Hodges 2011). These energies result in penetration depths of up to 100 nm over which the grains become amorphized at exposure times of close to 100 yr (Keller & McKay 1997). The disruption of the crystal lattice by ionizing radiation creates lattice vacancies and interstitials that may serve as effective catalytic sites for the recombination of two hydrogen atoms to form molecular hydrogen (H_2) or a reaction between trapped hydrogen and free oxygen atoms (Chatelain et al. 1970)

to possibly form H_2O) and/or OH (Managadze et al. 2011). Both mechanisms, along with the potential formation of Si–O–H functional groups, can be induced via nonequilibrium, high energy processes and by the diffusion of thermalized hydrogen atoms together with tunneling (Kuwahata et al. 2015). At Earth's distance from the Sun, the density of solar protons is 6 to 8 $\text{H}^+ \text{cm}^{-3}$ traveling at an average velocity of 450 km s^{-1} , although these values vary based upon solar activity (Starukhina & Shkuratov 2000; Poppe et al. 2013). Since the Moon only possesses an atmosphere of volatiles with virtually infinite mean free paths, i.e., an exosphere, the surface is entirely exposed to the solar wind. Many factors affect the local variability of solar wind levels at the surface but considering the Moon's distance from the Sun it receives an average incident flux of about $3 \times 10^8 \text{ H}^+ \text{cm}^{-2} \text{s}^{-1}$. At this rate, a saturation level of irradiation damage within a lunar regolith grain (reaching a dose of $\sim 10^{18} \text{ H}^+ \text{cm}^{-2}$) is typically reached after a period of only 100 yr (Starukhina 2006). However, micrometeorites and larger impacts garden the upper surface. The regolith reworking depth by micrometeorites is estimated to be close to $2 \mu\text{m}$ over 100 yr based on numerical modeling with a 99% chance of 100 turns (Costello et al. 2018) and ^{26}Al analyses of some lunar drill cores (Fruchter et al. 1977). Based on the analysis of drive tube cores collected during Apollo 17, it would take approximately 14 million years for the upper centimeter to be mature and the upper 50 cm would be mature within approximately 450 million years (Morris 1978; Morris et al. 1978). A more recent analysis by Speyerer et al. (2016) used temporal imaging of lunar impact crater sites to determine a gardening rate 100 times faster than the models by Morris et al. This discrepancy could be explained by the work done by Kulchitsky et al. (2018) which demonstrates that even partially buried grains can receive solar wind bombardment, thus decreasing the turnover timescales predicted from Apollo core samples. This means that on a relatively short geologic timescale the upper tens of centimeters should be

⁴ Current address: Department of Physics, Washington University, St. Louis, MO 63130, USA.

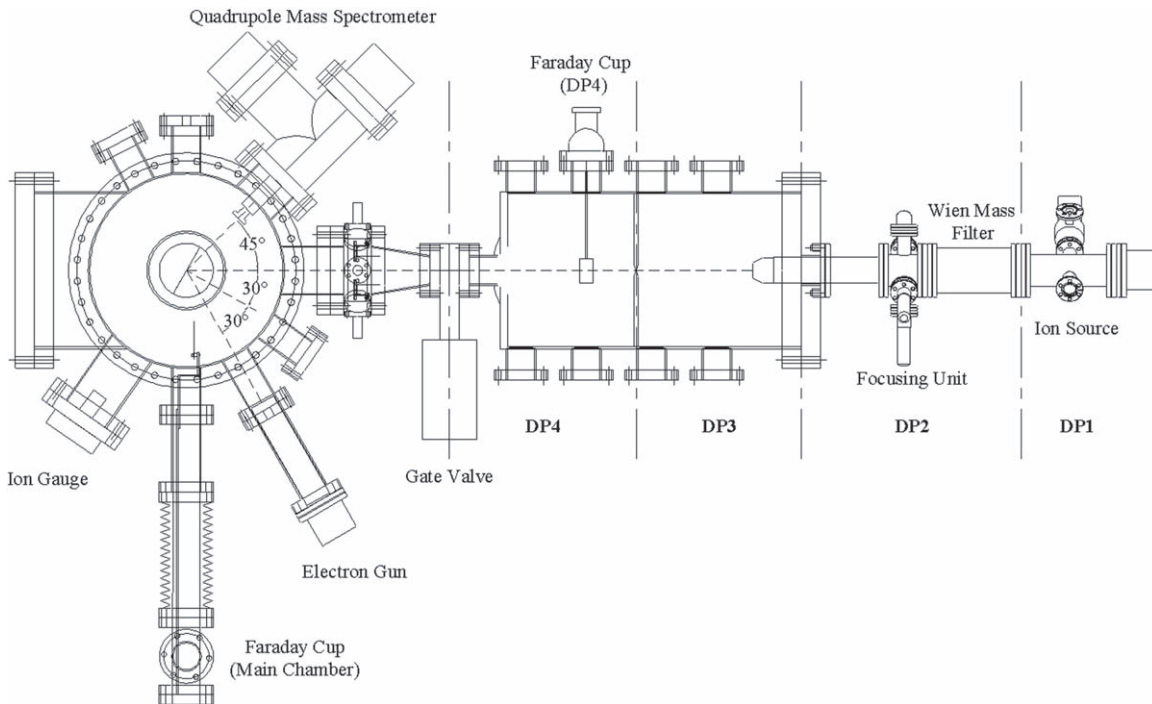


Figure 1. Top view of the experimental setup including the differentially pumped regions of the charged particle source.

saturated with solar wind implanted hydrogen. Thus, the concentration of molecular hydrogen in the exosphere is likely in a steady state condition, which is bound by the local flux of the solar wind and the temperature of the regolith (Hurley et al. 2017). The source of hydrogen is affected by diurnal variation and could explain changes in OH measurements (Clark 2009; Pieters et al. 2009; Sunshine et al. 2009).

Here, we conduct laboratory experiments employing deuterium ions as a proxy of hydrogen ions to simulate the interaction between lunar silicates and the solar wind and observe the temperature dependence of the formation of molecular deuterium from 10–250 K. Our method using deuterium ions is to discriminate between products formed as a result of the irradiation (D_2) compared to residual gases, in particular traces of molecular hydrogen (H_2), which are present in any vacuum chamber as the result of outgassing from the stainless steel material of the recipient. The present study experimentally demonstrates the key role of lunar silicate minerals to efficiently store molecular deuterium and how this process depends on the temperature. The capability of silicates to store and to effectively release molecular deuterium upon annealing provides solid experimental evidence that the solar wind represents a key source of molecular hydrogen in the tenuous lunar atmosphere, thus improving our understanding of the origin of tenuous exospheres not only of the Moon, but of airless bodies in our solar system in general.

2. Experimental Methods

To simulate the interaction of solar wind protons with the lunar regolith experimentally, we exposed San Carlos olivine ($[Mg_{1.8}Fe_{0.2}]SiO_4$, $<45 \mu m$) samples to a 5 keV D_2^+ molecular ion beam for a total fluence of $(1.17 \pm 0.06) \times 10^{18}$ deuterium nuclei cm^{-2} , equivalent to 130 ± 10 yr of irradiation at the lunar surface on average, under ultra-high vacuum conditions at temperatures ranging from 10–250 K (Figure 1, Table 1).

Table 1
Parameters for the Ion Irradiation Source

Parameter	Value
Kinetic energy of the ions (keV)	5.0
Ion flux ($cm^{-2} s^{-1}$)	$(1.25 \pm 0.06) \times 10^{13}$
Irradiated area (cm^2)	1.10 ± 0.2
Irradiation time (minutes)	780
Total deuterium nuclei (cm^{-2})	$(1.17 \pm 0.06) \times 10^{18}$
Solar wind proton flux on Moon ($cm^{-2} s^{-1}$) (1)	$(3.0 \pm 0.5) \times 10^8$
Simulated time (year)	130 ± 10

Reference. (1) Blanford et al. (1986).

Olivine has been widely used in previous studies to simulate space weathering effects on the Moon as a proxy of lunar material (Lord 1968; Loeffler et al. 2009; Burke et al. 2011; Djouadi et al. 2011; Zhu et al. 2019). The experiments were conducted within a stainless steel ultrahigh vacuum (UHV) chamber, evacuated to $(2.0 \pm 0.5) \times 10^{-10}$ mbar using oil-free turbomolecular pumps backed by dry scroll pumps (Ennis et al. 2011; Turner et al. 2016; Crandall et al. 2017). Samples were prepared by grinding the olivine to a fine powder and dry sieving the powder over a silver wafer ($3.1 \times 3.1 cm^2$) before pressing it onto the wafer using a hydraulic press. This method works well to produce a uniform and smooth olivine surface that completely covers the silver substrate, resulting in a sample mass of 0.8 ± 0.1 g and a thickness of approximately $250 \mu m$. The wafer was affixed to a rotatable copper cold finger (CTI-Cryogenics Cryodyne 1020, compressor: CTI-Cryogenics 9600) and a thin layer of indium foil was placed between the silver substrate and the cold finger to ensure good thermal conductivity. A Lakeshore DT-470 silicon diode sensor mounted near the substrate was used to monitor the temperature of the sample, which can be controlled within the range of 10–300 K by a 25Ω heater cartridge powered by a Lakeshore 336 temperature controller.

A quadruply differentially pumped ion source (SPECS IQE 12/38), supplied with a 4.0×10^{-3} mbar base pressure of high-purity molecular deuterium gas (D_2 : 99.999%; Icon Isotopes), produced the charged particle beam. With our particular ion source, molecular deuterium (D_2^+) ions are produced at fluxes two orders of magnitude higher compared to D^+ ions from the same source gas. It has been demonstrated that upon impact on the silicate surface, each molecular deuterium ion (D_2^+) dissociates resulting in implantation of a deuterium atom (D) and a deuteron (D^+ ion), each possessing 2.5 keV kinetic energy on average (Sigmund et al. 1996; Wieser et al. 2002; Kato et al. 2015), which is comparable to the range of the kinetic energy of solar wind particles of 1–2 keV amu^{-1} . It shall be noted that previous experimental studies demonstrated that molecular ions such as H_2^+ and even O_2^+ with kinetic energies larger than 1.9 keV and 2.9 keV, respectively, are completely dissociated upon interaction with solid surfaces (Wieser et al. 2002; Kato et al. 2015). Based on these experimental studies, since the present experiments are conducted with 5 keV D_2^+ , the survival probability of D_2^+ inside the olivine is zero. Only if low energy ions such as D_2^+ interact with metal surfaces, an electron can be transferred from the metal to the D_2^+ thus initially generating electronically excited D_2 , which is scattered back from the surface into the gas phase, but not inside the solid (Müller et al. 1993; Krischok et al. 1999; Lorente et al. 1999).

Located after the ionization and extraction regions of the ion source, a Wien mass filter separated unwanted atomic deuterium (D^+) and trideuterium (D_3^+) ions to produce a monoenergetic beam of 5 keV molecular deuterium ions (D_2^+) directed at the substrate. After passing through the mass filter, ions travel through three additional differentially pumped regions held at 1.6×10^{-6} , 4.7×10^{-8} , and 2.7×10^{-9} mbar, which are in place to maintain a pressure of low 10^{-10} mbar in the main chamber while the ion source is in operation. A Faraday cup in the main chamber measured the total ion current of the ions at the sample. This operation scans the ion beam over a sample area of $1 \times 1 \text{ cm}^2$ at a current of $2000 \pm 100 \text{ nA}$.

Six sets of experiments were carried out where separate olivine samples were held isothermally during irradiation at 10, 40, 80, 120, 200, and 250 K (one sample at each temperature), after which the samples were heated to 300 K at a ramp rate of 1 K min^{-1} (temperature programmed desorption; (TPD)). During this period, the controlled heating of the sample induces the diffusion of deuterium atoms, which are trapped within the olivine during irradiation, and also of molecular deuterium. During this process, deuterium atoms can recombine to molecular deuterium with the excess energy from the formation of a deuterium–deuterium bond released to the surrounding mineral thus stabilizing molecular deuterium. As these volatiles diffuse out of the sample, the gases are ionized via electron impact by a quadrupole mass spectrometer (QMS) yielding a mass-to-charge (m/z) ion signal (current) at $m/z = 4$ that is directly proportional to the partial pressure and hence number density of each species in the gas phase. The results from this TPD are compared to blank experiments, in which all experimental conditions are repeated save that no ion beam is introduced to the chamber.

A Balzer QMG 422 electron impact quadrupole mass spectrometer operating in the residual gas analyzer mode with electron impact energies of 100 eV at a 0.7 mA emission current and secondary electron multiplier operated at 3000 V was used to quantify the deuterium yield with the help of a leak valve. By calibrating the instrument, we can quantify the

number of volatile molecules escaping an irradiated solid during TPD. To do so, a positive shut-off capillary calibrated leak valve (Vacuum Technologies Incorporated) was connected to a deuterium gas reservoir and to the ultra-high vacuum chamber; this device provided a stable leak rate (Q) of 1.49×10^{-6} mbar L s^{-1} of deuterium gas into the chamber. The number of leaked deuterium molecules (n_{D_2}) is determined by Equation (1), where R and T represent the gas constant ($8.314 \text{ J K}^{-1} \text{ mol}^{-1}$) and temperature (293 K), respectively.

$$n_{D_2} = \frac{\int_0^t Q dt}{RT}. \quad (1)$$

Since the QMS signal is an amplified current generated by only those volatiles which enter the ionization source of the instrument, we need to determine the proportionality constant (K_{QMS}) between the number of deuterium molecules (n_{D_2}) escaping and the molecular ion current in A ($m/z = 4$, I_{D_2}). This is defined via Equation (2) with the time (t) in seconds and was determined to be $(8.95 \pm 0.24) \times 10^{19} \text{ molecules C}^{-1}$:

$$K_{\text{QMS}} = \frac{n_{D_2}}{\int_0^t I_{D_2} dt}. \quad (2)$$

The deuterium molecules detected during the TPD in the gas phase ($n_{D_2}(\text{TPD})$) was derived based on this constant and the current of the $m/z = 4$ signal measured by the SEM of the mass spectrometer ($I_{D_2}(\text{TPD})$) via Equation (3):

$$n_{D_2}(\text{TPD}) = K_{\text{QMS}} \int_0^t I_{D_2}(\text{TPD}) dt. \quad (3)$$

For comparison, ion trajectories through the sample were modeled using the Stopping and Range of Ions in Matter (SRIM) Monte Carlo program (Ziegler et al. 2010). A density of 3.35 g cm^{-3} was used for San Carlos olivine ($[\text{Mg}_{1.8}\text{Fe}_{0.2}]\text{SiO}_4$) and the layer was given a width of 300 nm. Deuterium was selected for the simulated ions with a mass of 2 amu and an energy of 2.5 keV. To calculate the damage of the substrate and the implantation profile, we selected “Detailed Calculation with Full Damage Cascades” for the TRIM calculation method and simulated a total of 99,999 trajectories. Results of these simulations calculated the average penetration depth to be $39 \pm 4 \text{ nm}$.

3. Results and Discussion

3.1. Lunar Environment Simulations

Figure 2(a) depicts the results from the TPD phase plotting the signal at $m/z = 4$, which is assigned to the formation of molecular deuterium (D_2), at distinct temperatures. Each sample exhibited an increased rate of D_2 release as the temperature increased to 300 K at which point the samples were held isothermally for three hours and the D_2 signal decreased exponentially. No D_2 formation was observed in the blank experiments during the TPD phase revealing that deuterium gas from the ion source chamber does not contribute to any background signal. These graphs visualize qualitatively that as the temperature increases from 10 to 250 K, less molecular deuterium is being released from the minerals during the warm up into the gas phase. This suggests that as the temperature rises, the capability of the silicate to store molecular deuterium is diminished. Since our QMS is calibrated, we integrated the signal intensity at $m/z = 4$ to quantify the total amount of deuterium molecules produced during the TPD phase (Figure 2(b), solid line). The data points

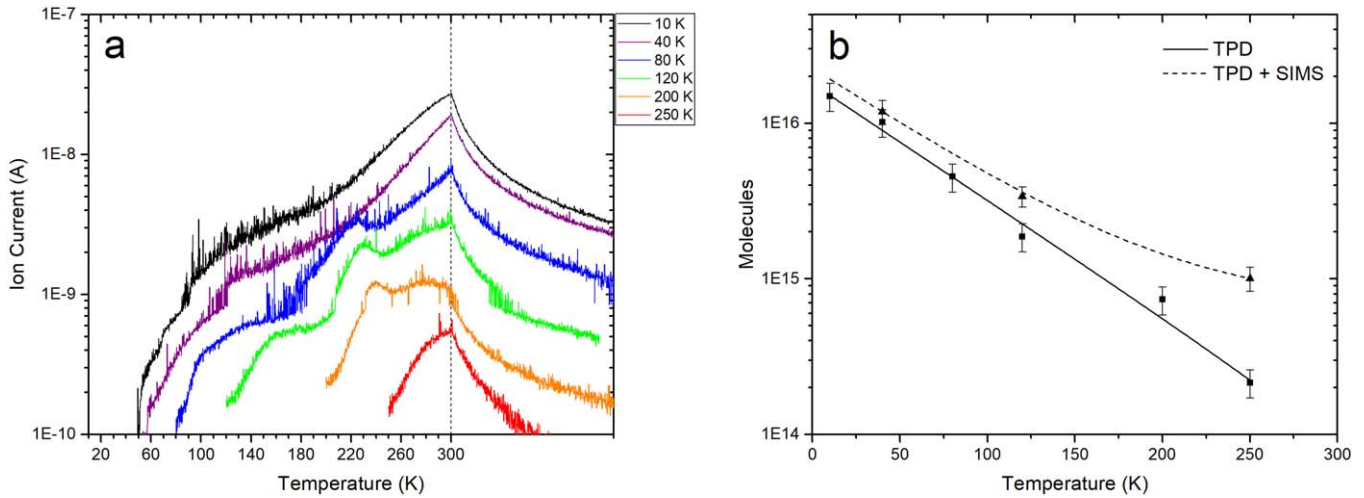


Figure 2. (a) Quantification of D_2 detected via the parent molecular ion at mass-to-charge $m/z = 4$ as a function of irradiation temperature. After the irradiation, each sample underwent TPD to 300 K (dotted line), at which point the sample was held isothermally for three hours. (b) Total number of D_2 molecules detected during TPD (solid line) from various irradiation temperatures as derived by integration of signal at mass-to-charge $m/z = 4$ exploiting a calibrated mass spectrometer. After TPD, additional deuterium was detected still trapped inside via SIMS analysis. Assuming this amount is completely converted to D_2 upon release, the maximum yield of D_2 molecules is represented by the dashed line. The error bars were calculated based on the uncertainty of the irradiation flux and error propagation of the calibration of the mass spectrometer.

could be fitted using the function defining the number of molecules $N = (1.80 \times 10^{16})e^{-\frac{T}{58.02}} - 1.87 \times 10^{13}$, where T defines the irradiation temperature in kelvin (K). The results support the aforementioned qualitative observations. As the irradiation temperature increases, the production of D_2 and hence capability to store deuterium in the silicates decreases. Since the diffusion of atomic and molecular deuterium within the silicate is enhanced as the temperature is raised, the reduced storage yield at higher irradiation temperatures is likely the effect of an enhanced diffusion of atomic deuterium and reaction to molecular deuterium followed by diffusion of the latter out of the silicates into the gas phase during the irradiation. This in turn leaves fewer deuterium atoms and molecules to be stored inside the minerals at, for instance, 250 K versus 10 K. Furthermore, accounting for the irradiation current, exposure time, and average backscattering of the ions calculated by SRIM, we determine the total number of deuterium nuclei implanted into the silicate target to be $(1.09 \pm 0.05) \times 10^{18}$ (Table 2). From the experiments, $(1.49 \pm 0.27) \times 10^{16}$ deuterium molecules were detected thus equating to an efficiency of $2.73\% \pm 0.51\%$ of the atomic deuterium storage at 10 K as derived from the gas phase deuterium molecules. Finally, it is important to note that in each experiment, no increase in the signal of $m/z = 20$ (D_2O) compared to the blank was observed in the irradiation and TPD phases. Consequently, if deuterated water formed from the interaction of deuterium ions with olivine and diffused out of the sample, it is below the detection limit of the spectrometer of approximately 10^8 molecules s^{-1} .

3.2. Ion Microprobe Analysis of Irradiated Grains

Having detected D_2 in the TPD phase, we now explore if the silicates still store deuterium at 300 K. Three samples, which were irradiated at temperatures relevant to the lunar surface at high to mid latitudes (40, 120, and 250 K), were analyzed by a CAMECA SIMS 1280 ion microprobe at the W. M. Keck Cosmochemistry Laboratory (Honolulu, HI) to measure the $D/^{18}O$ ratio as a function of depth. The samples were removed

Table 2
Quantified Deuterium Molecules (N) in the TPD Phase

Irradiation Temperature (K)	Deuterium Molecules (N)	Percent Efficiency ^a
10 (Blank)	N/A	N/A
10	$(1.49 \pm 0.27) \times 10^{16}$	2.55 ± 0.47
40	$(1.02 \pm 0.18) \times 10^{16}$	1.74 ± 0.32
80	$(4.54 \pm 0.81) \times 10^{15}$	0.78 ± 0.14
120	$(1.87 \pm 0.33) \times 10^{15}$	0.32 ± 0.06
200	$(7.35 \pm 1.30) \times 10^{14}$	0.13 ± 0.02
250	$(2.15 \pm 0.38) \times 10^{14}$	0.04 ± 0.01

Note.

^a Number of detected deuterium molecules (TPD phase) divided by the implanted molecular deuterium ions multiplied by 100.

from the UHV chamber and stored in steel containers at low 10^{-6} mbar and 300 K for several days before the SIMS analysis was carried out. Cesium ions (Cs^+) at 10 keV were rastered over eight analysis sites per sample with a $50 \times 50 \mu m^2$ area while sputtered material was monitored for concentrations of D and ^{18}O for 200 cycles. These investigations revealed that ^{18}O concentrations were stable regardless of depth so a $D/^{18}O$ ratio provides the most accurate results to determine the depth-dependent deuterium concentrations. Up to 80 profiles from each sample were averaged and compared (Figure 3). A comparison of the peak maxima of the depth profiles with the results from the SRIM Monte Carlo calculations suggests a sputtering rate of about 1 nm per cycle. We note that there are certain limitations to the modeling capabilities of these simulations. First, SRIM only considers an amorphous solid and thus cannot account for channeling effects in crystalline solids, like the olivine grains used in these experiments, which in some cases can result in enhanced diffusion. Second, SRIM has been shown to be inaccurate in calculating sputtering yields of target atoms and stopping powers of solids, particularly for low energy ions (<10 keV) (Wittmaack 2004; Hofsäss et al. 2014; Szabo et al. 2018). Taking an average value of the $D/^{18}O$

Table 3
Parameters for the Quantification of D₂ Trapped in Samples at 300 K via SIMS

Parameter	Value		
Density (g cm ⁻³)	3.36 ± 0.20		
Molar mass (g mol ⁻¹)	146.40		
Irradiated area (cm ²)	1.1 ± 0.2		
Depth of SIMS site (m)	(2.00 ± 0.40) × 10 ⁻⁵		
Exposed volume (cm ³)	(2.20 ± 0.48) × 10 ⁻⁵		
Mass of olivine (g)	(7.38 ± 0.16) × 10 ⁻⁵		
¹⁸ O atoms in exposed volume	(2.45 ± 0.54) × 10 ¹⁵		
O atoms in exposed volume	(1.21 ± 0.27) × 10 ¹⁸		
	40 K	120 K	250 K
Average D/ ¹⁸ O ratio	1.41 ± 0.49	1.24 ± 0.29	0.65 ± 0.16
Deuterium molecules stored	(1.72 ± 0.42) × 10 ¹⁵	(1.52 ± 0.39) × 10 ¹⁵	(7.92 ± 2.20) × 10 ¹⁴

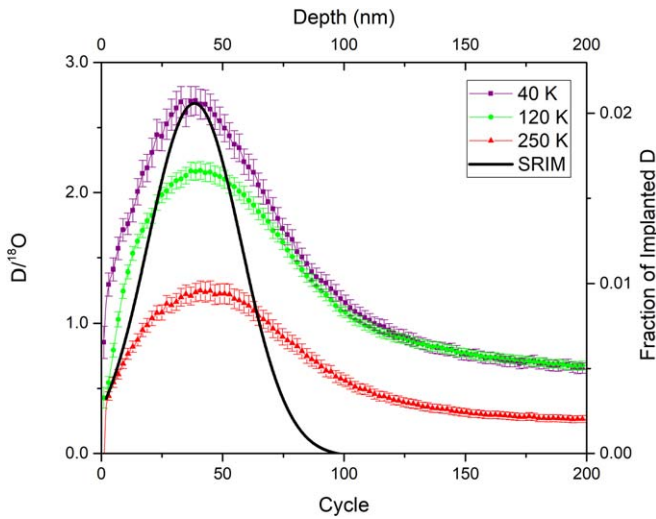


Figure 3. Depth profiles of the D/¹⁸O ratio determined by SIMS for samples irradiated at 40, 120, and 250 K, with error bars shown as the standard error of the mean. The lower *x*-axis designates the raster cycle number. These profiles are compared with the calculated irradiation depth profile from SRIM (black curve) of implanted deuterium ions in olivine, with the upper *x*-axis depicting depth from the irradiated surface. Aligning the experimental curves with the SRIM calculation indicates that the sputtering rate of the ion microprobe is essentially 1 nm cycle⁻¹.

ratio over the range for each profile, the amount of deuterium atoms still trapped inside the samples at the time of SIMS analysis can be quantified.

These observations can be rationalized by the following arguments. First, the width of the simulated depth profile (SRIM) is narrower than the experimentally obtained profiles at 40, 120, and 250 K. This is likely the effect of the thermal diffusion of the deuterium atoms within the minerals. SRIM does not include temperature dependent, thermal diffusion processes, but only energy transfer processes from the implant to the atoms in the solid within the binary collision approximation at 0 K (Ziegler et al. 2010). This in turn terminates the trajectory of the implant at a defined kinetic energy of 0.5 eV; at this time, the implanted species comes to rest in the simulated solid. However, under “real” conditions, these species diffuse thus leading to a broader distribution compared to the SRIM simulated profile. The inward diffusion of deuterium in particular is observed experimentally in all three samples revealing significant sputtering yields at depths beyond 100 nm, i.e., the maximum penetration depth determined

by SRIM calculations. We also observe that the FWHM of the peaks are essentially the same. This could be due to ion channeling effects of the crystalline olivine early in the irradiation phase. These effects allow ions to penetrate deeper into the solid than what is predicted by calculations since the crystalline structure governs their trajectories. As the olivine reaches the damage saturation point, the outer rim of the grain becomes completely amorphized, increasing the barrier to diffusion for the trapped deuterium atoms. This could explain why the concentration gradients of trapped deuterium appear the same, but the actual concentrations are determined by irradiation temperature.

Second, while some broadening of deuterium may occur during the physical sputtering process from the SIMS analysis, the sputtering profiles reveal that as the temperature is raised from 40 to 250 K, less deuterium is retained in the silicates. This result correlates with the aforementioned finding that with increasing temperature, the diffusion of deuterium throughout the solid and release into the gas phase translates into a significantly reduced storage capacity of the silicates as the temperature of the silicates is enhanced. Second, accounting for the irradiation area, the density of the olivine, the D/¹⁸O ratio, the calculated penetration depth, and the fraction of naturally occurring ¹⁸O (Tables 1 and 3; Figure 3), the amount of deuterium still trapped in the samples at 300 K can be determined and added to the deuterium released in the TPD phase (Tables 2 and 3). The overall yields are plotted in Figure 2(b) (dashed line) and can be fitted with the function $N = (2.19 \times 10^{16})e^{-\frac{T}{59.8}} + 6.73 \times 10^{14}$ with N defining the number of deuterium molecules and T the temperature in kelvin at which the sample was irradiated.

4. Astrophysical Implications and Conclusion

The present study provides compelling evidence and authenticates the proof-of-concept on the formation, storage, and liberation of molecular deuterium in and from olivine upon deuterium ion implantation over the range of 10–250 K, effectively simulating solar proton implantation into lunar silicates over a time span of 130 ± 10 yr. In the lunar environment, surface temperatures can range from 26 K in permanently shadowed craters near the poles (Vasavada et al. 2012) to 380 K in equatorial regions at midday (Paige et al. 2010a). As evidenced by the SIMS analysis, even at 300 K, the ion implanted olivine still stores deuterium; hence, we conclude that even at the highest lunar temperatures, the regolith grains would still be highly hydrogen enriched. This was found to be the

case with regolith samples returned from the Apollo missions (Hintenberger et al. 1970). On the Moon, the thermal processing of the regolith as the night cycles to day allows trapped hydrogen atoms to diffuse through the silicate thus recombining to molecular hydrogen (H_2) that contributes to the total concentration of molecular hydrogen in the lunar exosphere. These investigations signify the very first step toward a systematic comprehension on the formation and release of molecular hydrogen from lunar silicates and its contribution to the lunar exosphere. As for every simulation study, no single laboratory experiment can mimic the chemical and physical complexity of the lunar environment simultaneously. The laboratory simulation experiments reveal a fraction of deuterium conversion from the solar wind proxy to molecular deuterium of up to $3.51\% \pm 0.55\%$ accounting for the deuterium released in the TPD phase and stored at 300 K as determined via the SIMS analysis. This yield is lower than the estimated efficiency by Hurley et al. (2017) proposing that at close to 10% of the incoming solar wind protons would need to be converted to molecular hydrogen (H_2) to account for the observed molecular hydrogen density of 1200 cm^{-3} in the lunar exosphere. However, the kinetic energy distribution of hydrogen as it leaves a regolith grain represents a critical unknown in Hurley's model; this might critically reduce the required yield to a few percent as observed experimentally in our study.

The aforementioned data demonstrate also that the irradiated olivine in our simulation experiments still stores deuterium at 300 K, which can be released by micrometeorite impact on the lunar surface reaching peak temperatures of close to 1500 K. Lord (1968) demonstrated that for single-crystal San Carlos olivine nodules irradiated with 2 keV protons at 300 K, the release of trapped hydrogen continues well above 800 K. The author suggested that protons are neutralized upon impact and may bond to oxygen atoms in the lattice forming hydroxyl functional groups as supported by more recent infrared studies (Managadze et al. 2011). Demyk et al. (2004) exposed that the irradiation of crystalline silicates with 10 keV H^+ ions at a fluence of $10^{18} \text{ ions cm}^{-2}$ resulted in changes of the infrared spectrum with two bands emerging at 9.7–10.3 μm and 17–18 μm as attributed to the stretching and bending modes of the Si–O and O–Si–O bands in amorphized silicates. Experiments by Schaible & Baragiola (2014) revealed that the irradiation of San Carlos olivine with 5 keV H^+ ions at 295 K produced a broad band at 2.8 μm , which is characteristic of O–H stretching. By calculating the column density of the OH functional groups formed during irradiation, it was determined that the OH yield per implanted ion is initially as high as 0.9 OH bonds/proton and decreases to a saturation point at higher fluences. Thus, to release the chemically bound hydrogen, higher temperatures than those necessary for diffusion alone are required to break the O–H bonds. Further experiments are clearly necessary to explore the question of how the conversion yield depends on the texture, grain size, and chemical composition of the silicates within the lunar soil. Likewise, energetic solar photons and in particular heavier solar wind ions, although having fluxes at least one order of magnitude lower than solar wind protons, predamage the silicates thus generating defects in which hydrogen might be stored more efficiently (Demyk et al. 2004; Schaible & Baragiola 2014). In addition, constraints on the average concentration of stored hydrogen in the lunar regolith are still largely misrepresented. Novel methods measuring protons ejected by galactic cosmic

rays are expected to promote a better understanding of the diurnal variation of hydrogen on the surface of the Moon (Schwadron et al. 2018).

Nevertheless, despite these open questions, our proof-of-concept study defines a critical benchmark toward better comprehension on the origin, storage, and release of hydrogen in lunar silicates and its contribution to the lunar exosphere and on other airless bodies in our solar system such as Mercury. These data also reveal that cold traps on the Moon store molecular hydrogen more efficiently than regions at elevated temperatures (Figure 2(b)) thus providing a possible explanation of the low neutron albedo of the cold traps in the Moon as observed by the *Lunar Crater Observation and Sensing Satellite* where subsurface temperatures are estimated to be 38 K (Starukhina 2006; Paige et al. 2010b). The presence of trapped deuterium within the amorphous rims of the olivine grains following irradiation suggests that silicate minerals are excellent materials for hydrogen trapping. In the lunar environment, surface temperatures can range from 26 K in permanently shadowed craters near the poles (Vasavada et al. 2012) to 380 K in equatorial regions at midday (Paige et al. 2010a). While we are limited to a maximum temperature of 300 K due to our experimental setup, we would expect that even at the highest lunar temperatures, regolith grains would still be highly hydrogen enriched within the amorphous rims. This was found to be the case with regolith samples returned from the Apollo missions (Hintenberger et al. 1970). The thermal processing of the regolith as the night cycles to day allows trapped hydrogen atoms to diffuse through the amorphous rims and recombine to form molecular hydrogen (H_2) that contributes to the total concentration of the lunar exosphere.

The authors wish to thank Dr Norbert Schorghorfer (Planetary Science Institute, Arizona), Dr Gary Huss (W. M. Keck Cosmochemistry Laboratory), Dr Kazuhide Nagashima (W. M. Keck Cosmochemistry Laboratory), and Dr Dana M. Hurley (Johns Hopkins University) for discussions. This work was supported by NASA under grants NNX16AO79G, NNX14AI48G, and NNA14AB02A to the University of Hawai'i at Manoa (R.I.K., J.J.G.-D.).

ORCID iDs

Parker B. Crandall  <https://orcid.org/0000-0002-4585-5868>

Jeffrey J. Gillis-Davis  <https://orcid.org/0000-0002-4047-680X>

Ralf I. Kaiser  <https://orcid.org/0000-0002-7233-7206>

References

- Blanford, G., Børgeesen, P., Maurette, M., Möller, W., & Monart, B. 1986, *JGR*, **91**, 467
- Burke, D. J., Dukes, C. A., Kim, J. H., et al. 2011, *Icar*, **211**, 1082
- Chatelain, A., Kolopus, J. L., & Weeks, R. A. 1970, *Sci*, **168**, 570
- Clark, R. N. 2009, *Sci*, **326**, 562
- Colaprete, A., Sarantos, M., Wooden, D. H., et al. 2016, *Sci*, **351**, 219
- Costello, E. S., Ghent, R. R., & Lucey, P. G. 2018, *Icar*, **314**, 327
- Crandall, P. B., Göbi, S., Gillis-Davis, J., & Kaiser, R. I. 2017, *JGRE*, **122**, 1880
- Demyk, K., D'Hendecourt, L., Leroux, H., Jones, A. P., & Borg, J. 2004, *A&A*, **420**, 233
- Djouadi, Z., Robert, F., Le Sergeant d'Hendecourt, L., et al. 2011, *A&A*, **531**, A96
- Ennis, C., Bennett, C. J., Jones, B. M., & Kaiser, R. I. 2011, *ApJ*, **733**, 79
- Feldman, P. D., & Morrison, D. 1991, *GeoRL*, **18**, 2105

- Fruchter, J. S., Rancitelli, L. A., Lau, J. C., & Perkins, R. W. 1977, *LPSC*, **8**, 3595
- Gnaser, H. 1999, *Low-energy Ion Irradiation of Solid Surfaces* (1st ed.; Berlin: Springer)
- Hintenberger, H., Weber, H. W., Voshage, H., et al. 1970, *Sci*, **167**, 543
- Hodges, R. R. 2011, *GeoRL*, **38**, L06201
- Hofsäss, H., Zhang, K., & Mutzke, A. 2014, *ApSS*, **310**, 134
- Hurley, D. M., Cook, J. C., Retherford, K. D., et al. 2017, *Icar*, **283**, 31
- Kato, S., Tanaka, N., Sasao, M., et al. 2015, *JNuM*, **463**, 361
- Keller, L. P., & McKay, D. S. 1997, *GeCoA*, **61**, 2311
- Krischok, S., Müller, H., & Kempfer, V. 1999, *NIMPB*, **157**, 198
- Kulchitsky, A. V., Hurley, D. M., Johnson, J. B., Duvoy, P. X., & Zimmerman, M. 2018, *JGRE*, **123**, 972
- Kuwahata, K., Hama, T., Kouchi, A., & Watanabe, N. 2015, *PhRvL*, **115**, 133
- Loeffler, M. J., Dukes, C. A., & Baragiola, R. A. 2009, *JGRE*, **114**, E03003
- Lord, H. C. 1968, *JGR*, **73**, 5271
- Lorente, N., Teillet-Billy, D., & Gauyacq, J. P. 1999, *JChPh*, **111**, 7075
- Lucey, P. 2006, *RvMG*, **60**, 83
- Managadze, G. G., Cherepin, V. T., Shkuratov, Y. G., Kolesnik, V. N., & Chumikov, A. E. 2011, *Icar*, **215**, 449
- Morris, R. 1978, *Lunar and Planetary Science Conference 9, 2* (New York: Pergamon), 1801
- Morris, R. V., Gose, W. A., & Lauer, H. V., Jr., 1978, *Lunar and Planetary Science Conf. 9, 2* (New York: Pergamon), 2033
- Müller, H., Hausmann, R., Brenten, H., & Kempfer, V. 1993, *SurSc*, **284**, 129
- NASA 1973, *Apollo 17: Preliminary Science Report*, NASA SP-330, Vol. 330 (Washington, DC)
- Paige, D. A., Foote, M. C., Greenhagen, B. T., et al. 2010a, *SSRv*, **150**, 125
- Paige, D. A., Siegler, M. A., Zhang, J. A., et al. 2010b, *Sci*, **330**, 479
- Pieters, C. M., Goswami, J. N., Clark, R. N., et al. 2009, *Sci*, **326**, 568
- Poppe, A. R., Halekas, J. S., Sarantos, M., & Delory, G. T. 2013, *JGRE*, **118**, 1934
- Sarantos, M., Hartle, R. E., Killen, R. M., et al. 2012, *GeoRL*, **39**, L13101
- Schaible, M. J., & Baragiola, R. A. 2014, *JGRE*, **119**, 2017
- Schwadron, N. A., Wilson, J. K., Jordan, A. P., et al. 2018, *P&SS*, **162**, 113
- Sigmund, P., Bitensky, I. S., & Jensen, J. 1996, *NIMPB*, **112**, 1
- Speyerer, E. J., Povilaitis, R. Z., Robinson, M. S., Thomas, P. C., & Wagner, R. V. 2016, *Natur*, **538**, 215
- Starukhina, L. V. 2006, *AdSpR*, **37**, 50
- Starukhina, L. V., & Shkuratov, Y. G. 2000, *Icar*, **147**, 585
- Stern, S. A. 1999, *RvGeo*, **37**, 453
- Sunshine, J. M., Farnham, T. L., Feaga, L. M., et al. 2009, *Sci*, **326**, 565
- Szabo, P. S., Chiba, R., Biber, H., et al. 2018, *Icar*, **314**, 98
- Turner, A. M., Abplanalp, M. J., & Kaiser, R. I. 2016, *ApJ*, **820**, 127
- Vasavada, A. R., Bandfield, J. L., Greenhagen, B. T., et al. 2012, *JGRE*, **117**, E00H18
- Wieser, M., Wurz, P., Brüning, K., & Heiland, W. 2002, *NIMPB*, **192**, 370
- Wittmaack, K. 2004, *JAP*, **96**, 2632
- Zhu, C., Crandall, P. B., Gillis-Davis, J. J., et al. 2019, *PNAS*, **116**, 11165
- Ziegler, J. F., Ziegler, M. D., & Biersack, J. P. 2010, *NIMPB*, **268**, 1818